In situ sprayed NIR-responsive, analgesic black phosphorus-based gel for diabetic ulcer treatment

Jiang Ouyang[a,b,c,1], Xiaoyuan Ji[a,b,1], Xingcai Zhang[d,1], Chan Feng[a,b], Zhongmin Tang[a,b], Na Kong[a,b], Angel Xie[a,b], Junqing Wang[a,b], Xinbing Sui[e], Liu Deng[c], Younian Liu[c], Jong Seung Kim[f], Yihai Cao[g], and Wei Tao[a,b,2]

aCenter for Nanomedicine, Brigham and Women's Hospital, Harvard Medical School, Boston, MA 02115; bDepartment of Anesthesiology, Perioperative and Pain Medicine, Brigham and Women's Hospital, Harvard Medical School, Boston, MA 02115; cCollege of Chemistry and Chemical Engineering, Central South University, 410083 Changsha, Hunan, China; dJohn A. Paulson School of Engineering and Applied Sciences, Harvard University, Cambridge, MA 02138; eCollege of Pharmacy, School of Medicine, Hangzhou Normal University, 311121 Hangzhou, Zhejiang, China; fDepartment of Chemistry, Korea University, 02841 Seoul, Korea; and gDepartment of Microbiology, Tumor and Cell Biology, Karolinska Institute, Stockholm 171 77, Sweden

The treatment of diabetic ulcer (DU) remains a major clinical challenge due to the complex wound-healing milieu that features chronic wounds, impaired angiogenesis, persistent pain, bacterial infection, and exacerbated inflammation. A strategy that effectively targets all these issues has proven elusive. Herein, we use a smart black phosphorus (BP)-based gel with the characteristics of rapid formation and near-infrared light (NIR) responsiveness to address these problems. The in situ sprayed BP-based gel could act as 1) a temporary, biomimetic "skin" to temporarily shield the tissue from the external environment and accelerate chronic wound healing by promoting the proliferation of endothelial cells, vascularization, and angiogenesis and 2) a drug "reservoir" to store therapeutic BP and pain-relieving lidocaine hydrochloride (Lid). Within several minutes of NIR laser irradiation, the BP-based gel generates local heat to accelerate microcirculatory blood flow, mediate the release of loaded Lid for "on-demand" pain relief, eliminate bacteria, and reduce inflammation. Therefore, our study not only introduces a concept of in situ sprayed, NIR-responsive pain relief gel targeting the challenging wound-healing milieu in diabetes but also provides a proof-of-concept application of BP-based materials in DU treatment.

black phosphorus | fibrin gel | diabetic ulcer | wound healing | analgesic

Diabetic ulcer (DU), a chronic complication of diabetes mellitus, appears as chronic wounds (also referred to as open sores) that usually form on the feet and legs but sometimes also in other folds of skin (1). Given its tendency toward infection, ulceration, severe pains, and destruction of deep tissues (2), DU is the leading cause of nontraumatic limb amputations due to the damage of both macro- and microvascular neuropathy (3, 4). The main causes of DU include the following: 1) the hyperglycemic symptoms of diabetes induce microvascular endothelial cell (EC) damage, vasodilatory dysfunction, with subsequently reduced oxygen supply to tissues; 2) vascular dysfunction further leads to tissue ischemia and hypoxia, forming chronic wounds (5, 6); 3) the open sores, prolonged wound healing time, and hyperglycemic environment make the wounds more susceptible to infection (7); and 4) the aggravation of wound infection, in turn, promotes the reproduction of bacteria and delayed wound healing with severe pain (8, 9). Thus, promoting EC proliferation, activating angiogenesis, facilitating local neovascularization and peripheral blood flow (10, 11), reducing bacterial infection and inflammation (12), and relieving pain are critical in the treatment of DU and accelerating the healing of chronic wounds.

Current DU treatments extensively used in clinical practice include wound debridement, reducing infection, weight control, and patient education (12). These treatments can offer some pain relief and may help prevent infection. However, they have a minor therapeutic effect on accelerating wound healing. Although some new treatments like tissue engineering products, wound dressings, and wound autografts represent progress in therapy for chronic DU (10, 13–15), effective pain relief during DU treatments remains elusive. Despite these well-established wound treatments,

effective therapeutic approaches to chronic DU remain a major clinical challenge due to the combination of chronic wounds, impaired angiogenesis, persistent pain, bacterial infection, and exacerbated inflammation (16, 17). Therefore, an effective strategy to intelligently target and address all these DU-related issues is highly desirable.

Herein, we developed an in situ sprayed, near-infrared (NIR)-responsive, pain-relieving black phosphorus (BP)-based gel for the treatment of DU. The functionalized gel contains 1) US Food and Drug Administration (FDA)-approved fibrinogen and thrombin, which have unique merits including good biocompatibility, amenability to a simple spray-coating approach (18, 19), and wound healing through promoting angiogenesis; 2) BP nanosheets (NSs), which can easily degrade into nontoxic phosphate ions (20, 21) and act as effective photothermal agents (22); and 3) the FDA-approved anesthetic lidocaine hydrochloride (Lid). Acting as a temporary, artificial "skin," the engineered BP-based gel not only temporarily shields tissues from the external environment and promotes EC proliferation and vascularization but also provides a drug "reservoir" that can generate local heat under NIR laser (808 nm) irradiation to accelerate microcirculatory blood flow, trigger the release of Lid for "on-demand" pain relief (23), and eliminate bacteria and reduce inflammation via photothermal therapy (PTT) (24). Regardless of the different shapes or areas of the wounds, the developed technology can be quickly mixed and sprayed at the DU site to

Significance

How to achieve effective treatment of diabetic ulcer (DU) is still a major challenge in the clinic. Herein, we propose an effective strategy to perfectly address all the problems faced in the treatment of DU. A near-infrared–responsive black phosphorus-based sprayed fibrin gel capable of alleviating pain, eliminating bacteria, reducing inflammation, and promoting angiogenesis is developed. The promoting wound healing and pain relief effects in the diabetic mouse ulcer model indicate this gel is a valuable wound dressing for effective treatment of DU and other advanced wounds. We anticipate that this therapeutic strategy may be generalized for treating other disorders such as chronic inflammation and infections.

form wound-healing gels in situ. In addition, this approach can avoid the toxic effects associated with the systemic administration of drugs. Therefore, we provided the proof-of-principle evidence for the use of an in situ sprayed NIR-responsive pain-relief gel to support accelerated wound healing in DUs (Fig. 1).

Results

Characterizations of the BP-Based Gel. BP NSs were prepared based on a previously reported approach (25). Transmission electron microscopy (TEM) shows that the as-prepared BP nanostructures (average size ~180 nm) have a sheet morphology (Fig. 2*A*). High-angle annular dark-field scanning transmission electron microscopy confirmed the sheet structure, and energy-dispersive spectroscopy mapping revealed that the elements P and O were evenly distributed throughout the NSs (*SI Appendix,* Fig. S1*A*). Atomic force microscopy (AFM) further verified the ultrathin NS structure of BP (Fig. 2*B*), with a thickness of about 3.5 nm (Fig. 2*C*). Furthermore, the Raman spectrum showed that the peaks of BP NSs had a slight red shift compared to those of bulk BP, indicating the formation of BP NSs (Fig. 2*D*). To further investigate the chemical composition of the obtained BP NSs, X-ray photoelectron spectroscopy (XPS) and X-ray diffraction (XRD) were performed (23). Only C, P, and O were present in the full XPS spectrum, and the characteristic doublets of $2p_{1/2}$ and $2p_{3/2}$ in BP NSs were 131 eV and 130.1 eV, respectively (*SI Appendix,* Fig. S1 *B* and *C*). All of the XRD peaks of BP NSs matched the standard pattern of P closely (International Centre for Diffraction Data: 76 to 1,957) (*SI Appendix,* Fig. S1*D*), manifesting their high purity. All these findings demonstrate the successful preparation of BP NSs.

To obtain the gels used in this study, fibrinogen solutions with/without BP NSs were mixed with an equal volume of thrombin solution through simultaneous spraying (18). The digital photograph in Fig. 2*H* shows the successful formation of Gel and BP@Gel through a vial turnover test. The rheology test results further validated the hydrogel properties of Gel and BP@Gel. Over the whole frequency domain, the storage modulus (G′) of Gel and BP@Gel were always greater than their loss modulus (G″), even when the doped concentration of BP NSs was raised to 200 μg·mL^{-1}, indicating the hydrogel characteristics of Gel and BP@Gel (*SI Appendix,* Fig. S2). The corresponding photo of BP@Gel with different concentrations of BP NSs also demonstrates hydrogel characteristics (*SI Appendix,* Fig. S3). Subsequently, a scanning electron microscope (SEM) was employed to examine the microstructures of Gel and BP@Gel after freeze-drying. As shown in Fig. 2*E*, an obvious fibrin network structure

was observed in the sample of Gel, and the high-magnification SEM further confirmed that the formed fibers in fibrin were intertwined to generate the hydrogel structure (*SI Appendix,* Fig. S4). In the case of BP@Gel, it retained its fibrin network structure, with BP NSs homogeneously distributed in the hydrogel (*SI Appendix,* Fig. S5). A strong compositional contrast between BP NSs (sky blue) and hydrogel (dark blue) appears in the pseudo-color SEM image (Fig. 2*F*), further indicating the encapsulation of BP NSs in the Gel. Moreover, the results of energy-dispersive X-ray (EDX) analysis revealed the presence of C, O, N, and P in the BP@Gel (Fig. 2*G*), among which P originated from BP NSs, and C, O, and N can be attributed to the hydrogel. Moreover, several photographs were taken to characterize the gelation process and the reaction rate of the fibrinogen/thrombin gel with or without BP NSs. We found that the mixed solution containing fibrinogen and thrombin can form a hydrogel within 120 s (Fig. 2*I*). As shown in these images, the mixed solution initially showed an obvious solution state when the fibrinogen solution was mixed with a thrombin solution. Meanwhile, the gelation process of the mixture began from 60 s, and it was completely gelled at 120 s. Notably, the presence of BP NSs had some influence on the gelation time of fibrin gel. When the BP NSs (50 μg·mL^{-1}) were added to the mixture, the gelation time was extended to 150 s, and the gelation time was prolonged with the increase of BP NSs concentration.

BP-Based Gel Promotes the Proliferation of Endothelial Cells. Since hydrogels can serve as scaffolds for cell proliferation (26–28), we speculate that our hydrogel composed of thrombin and fibrinogen can be used as a scaffold for skin cell growth. We investigated the effects of Gel and BP@Gel on skin cell proliferation in vitro, using human umbilical vein ECs (HUVECs) as a model cell line. The proliferation of HUVECs on the surface of Gel or BP@Gel were significantly faster than on the glass substrate after 1 and 3 d of incubation (Fig. 3 *A* and *B*). Additionally, the cell gap between the hydrogel and glass substrate increased with time. Live/dead staining assay further confirmed the above results (*SI Appendix,* Fig. S6*A*). Interestingly, obvious cell differentiation behavior was observed after incubating HUVECs on the surface of Gel or BP@Gel (*SI Appendix,* Fig. S6*B*), demonstrating suitability for the growth of HUVECs. Afterward, 5-ethynyl-2′-deoxyuridine (EdU), a sensitive reagent used to label the nuclei of proliferating cells, was used to explore the detailed impact of gels on the proliferation of HUVECs (29). The results showed that the proliferation of HUVECs with bright green fluorescence treated with either Gel or BP@Gel was higher than in the control group. In addition, the quantitative analysis data demonstrated that
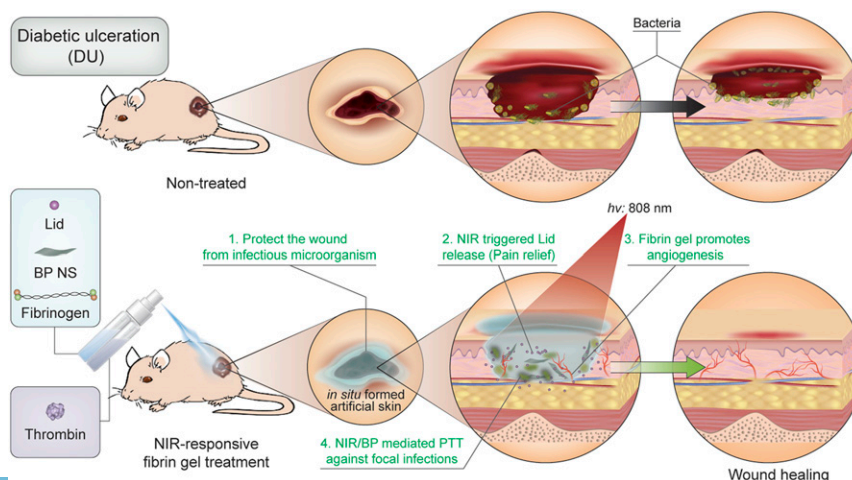

Fig. 1. Schematic illustration of in situ sprayed NIR-responsive, pain-relieving gel for accelerated wound healing in DU.
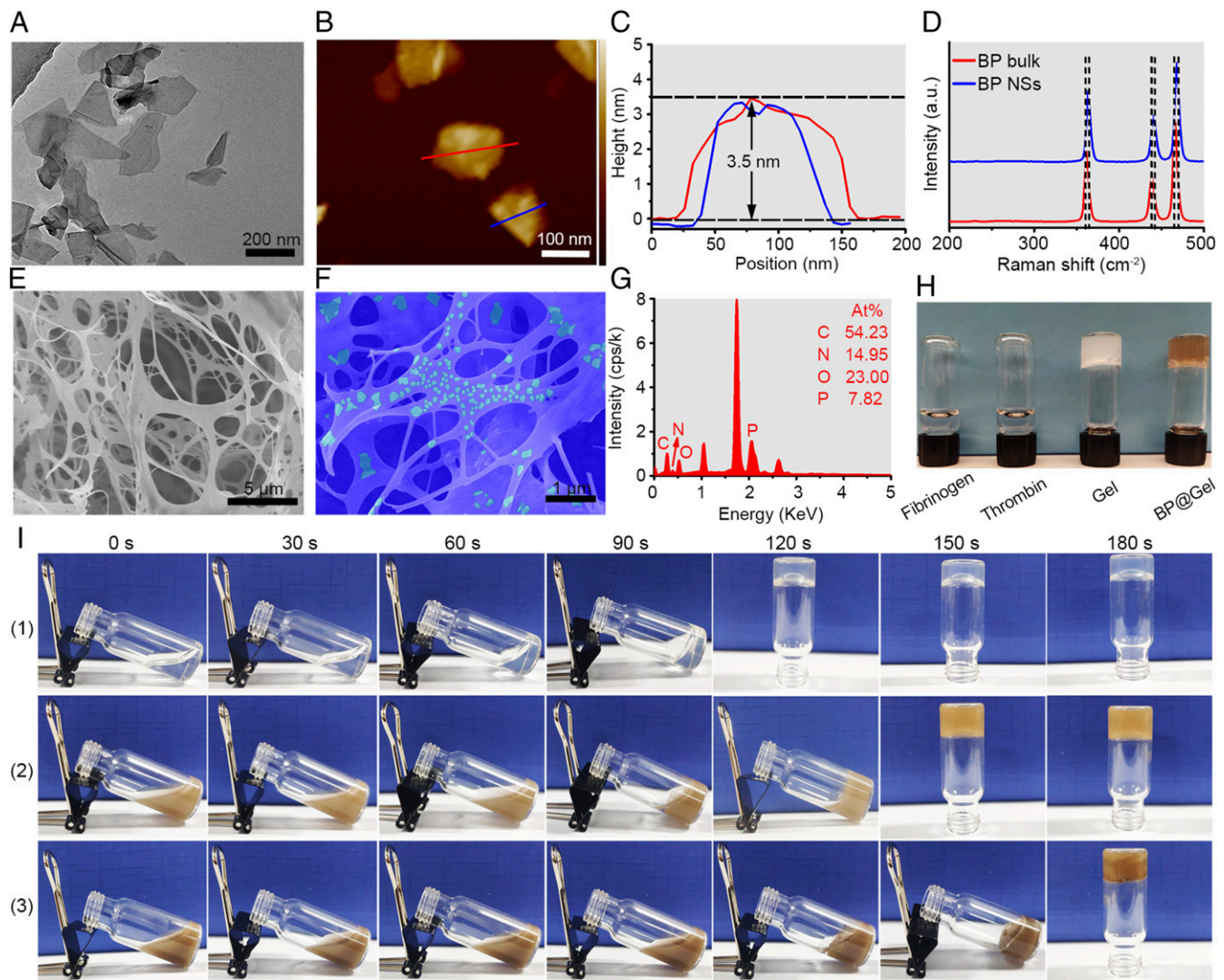
Ouyang et al.

Fig. 2. Characterizations of BP-based gel. (*A*) TEM image of BP NSs. (*B*) AFM image of BP NSs. (*C*) Thickness profile of BP NSs in *B*. (*D*) Raman spectrum of bulk BP and BP NSs. (*E*) SEM image of Gel. (*F*) Pseudocolor SEM image of BP@Gel. (*G*) EDX profile of BP@Gel. (*H*) Digital photograph of Gel and BP@Gel. (*I*) The gelation time of fibrinogen/thrombin gel with different BP NSs concentrations: (1) 0 $\mu g \cdot mL^{-1}$, (2) 50 $\mu g \cdot mL^{-1}$, and (3) 100 $\mu g \cdot mL^{-1}$.

HUVECs proliferated after incubation on the surface of Gel and BP@Gel by about 66.5% and 67.1%, respectively, while the proliferation of HUVECs in the control group was only 46.8% (Fig. 3 *C* and *D*). Subsequently, similar experiments were performed on Detroit 551 (D551) human fibroblast cells. After D551 were treated with Gel or BP@Gel, negligible proliferation was found in assays of cell viability (*SI Appendix*, Fig. S7 *A* and *B*), EdU nucleus labeling, or live/dead staining (*SI Appendix*, Fig. S7 *C–E*), all of which were almost the same as the control group. These results indicated 1) good biocompatibility of Gel and BP@Gel and 2) the selective proliferation of ECs compared to fibroblast cells.

Therefore, the regenerative ability of Gel and BP@Gel was further investigated using HUVECs. A scratch assay was executed to explore the impact of Gel or BP@Gel scaffolds on the migration of HUVECs. The scratch of HUVECs covering a 12-well plate was created via a pipette tip, which ensured a consistent "wound" width. Afterward, transwells loaded with hydrogel scaffolds were put into in the 12-well plate to evaluate the growth and migration of HUVECs. After 54 h of incubation, there was obvious cell migration in the scratch area and near

disappearance of the wound in both Gel and BP@Gel groups (Fig. 3*E*). The wound area in Gel and BP@Gel groups decreased dramatically by 67.9% and 69.8%, respectively, while only 38.8% of the wound decreased in the control group (Fig. 3*F*). The proliferation and migration among HUVECs induced by BP-based gel can be attributed to the fibrin generated through the cleavage of fibrinogen by thrombin, supporting improved wound healing.

BP-Based Gel Promotes Vascularization. Angiogenesis, the process of developing new capillaries from the original microvasculature, is an important stage in wound healing (30). This process involves the proliferation, migration, alignment, and germination of ECs, as well as the formation of cell-to-cell connections, tubular structures, and lumina (31). The extracellular matrix (ECM), which provides biochemical support to ECs, plays an important role during angiogenesis (32). Fibrin is a natural angiogenic agent that can also serve as a storage depot for growth factor during wound healing (33). We thus assessed the effect of Gel and BP@Gel on lumen formation through fibrin bead assays. After 2 d of incubation, HUVECs on the surface of beads began to sprout, and short as well as narrow rope-like structures
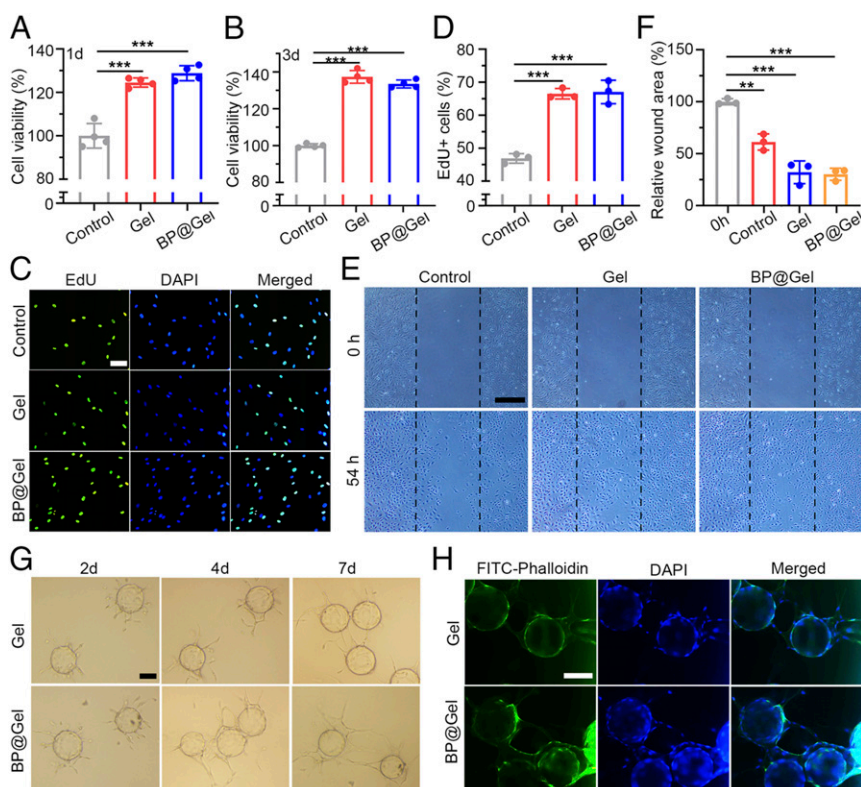
Ouyang et al.

www.manaraa.com

Fig. 3. BP-based gel promotes the proliferation and vascularization of ECs. Cell proliferation after HUVECs were incubated on the surface of Gel and BP@Gel for (*A*) 1 d and (*B*) 3 d. (*C*) Fluorescent images of EdU-labeled proliferating HUVECs incubated on Gel and BP@Gel for 72 h. Green, proliferating cells; blue, total cells. (Scale bar, 40 μm.) (*D*) Quantitative measurement of the EdU+ HUVECs. (*E*) Effects of Gel and BP@Gel on HUVEC migration. (Scale bar, 200 μm.) (*F*) Quantitative analysis of cell migration after HUVECs were treated with Gel and BP@Gel. (*G*) Formation of capillary-like sprouts differentiated by HUVECs in Gel and BP@Gel and their growth at 2, 4, and 7 d. (Scale bar, 100 μm.) (*H*) FITC-phalloidin and DAPI staining of formed capillary after 7-d incubation of HUVECs. (Scale bar, 100 μm.) **P < 0.01, and ***P < 0.001.

were noted. The rope-like structures continued to lengthen for several days. On the fourth day, obvious branches were found, indicating capillary-like structure (lumen) formation. It is noteworthy that by the seventh day adjacent blood vessels were crosslinked to form a vascular network (Fig. 3*G*). Afterward, DAPI (4′,6-diamidino-2-phenylindole) and fluorescein isothiocyanate (FITC)-phalloidin were used to stain the lumen to further confirm that the fibrin gel promoted the formation of a vascular network from HUVECs. As displayed in Fig. 3*H*, lumina with bright green fluorescence were surrounded by multiple cells, and neighboring branched lumens were anastomosed to form capillaries. These positive results applied to both Gel and BP@Gel. Conversely, the hydrogel composed of low-melting-point agarose and fibrinogen could not support HUVEC proliferation and angiogenesis at all (*SI Appendix*, Fig. S8), which was attributed to the absence of thrombin, which converts fibrinogen to fibrin. These results demonstrated that the BP-based gel served as an ideal ECM to facilitate HUVEC proliferation and angiogenesis to accelerate wound healing.

BP-Based Gel Eliminates Bacteria through Photothermal Effects. Since the DU wound is always exposed to the external environment, from formation to healing, the risk of external bacterial infection and serious delays in wound healing is high (3). Considering the potential of BP-based nanomaterials in PTT-mediated antibacterial effects (23, 34), we next investigated the in vitro antibacterial performance of BP@Gel, beginning with an evaluation of its photothermal effect under NIR laser irradiation. As displayed in Fig. 4*A*, the photothermal effect of BP@Gel was

correlated with the concentration of BP NSs. The temperature of the Gel increased by only 3.5 °C with NIR laser irradiation. However, the temperature of BP@Gel with a BP NSs concentration of 200 μg·mL^{-1} increased by 40.8 °C, a robust photothermal effect. Additionally, the photothermal effect of BP@Gel also showed obvious dependence on laser power (*SI Appendix*, Fig. S9*A*). Notably, after five cycles of NIR laser irradiation, BP@Gel retained a significant photothermal effect, indicating outstanding photothermal stability (*SI Appendix*, Fig. S9*B*). However, the rheological property of BP@Gel was drastically reduced after three cycles of irradiation (*SI Appendix*, Fig. S9*C*), suggesting that BP@Gel may be affected by local hyperthermia after repeated irradiation. Therefore, new and repeated treatments (i.e., spraying new BP-based gel) are suggested when a long-term therapy is required, which is also quite simple and convenient.

Subsequently, *Staphylococcus aureus* (SA) was selected as the model bacterium with which to study the PTT-mediated antibacterial activity of BP@Gel. After different treatments, the optical densities of an SA suspension at 600 nm (OD$_{600}$) were measured to assess bacterial activity. As can be observed in Fig. 4*B*, neither Gel nor BP@Gel had an obvious influence on bacterial growth, as levels were almost the same as in the control group. Bacterial growth was prominently suppressed in the group with BP@Gel and NIR laser irradiation, which was ascribed to the photothermal effect of BP@Gel. To further characterize the antibacterial activity of BP@Gel, an agar plate assay was performed (Fig. 4*C*). Bacterial colonies were negligible in the agar plate after treatment with BP@Gel and NIR laser irradiation; in other groups, a large number of bacteria survived. Quantitative
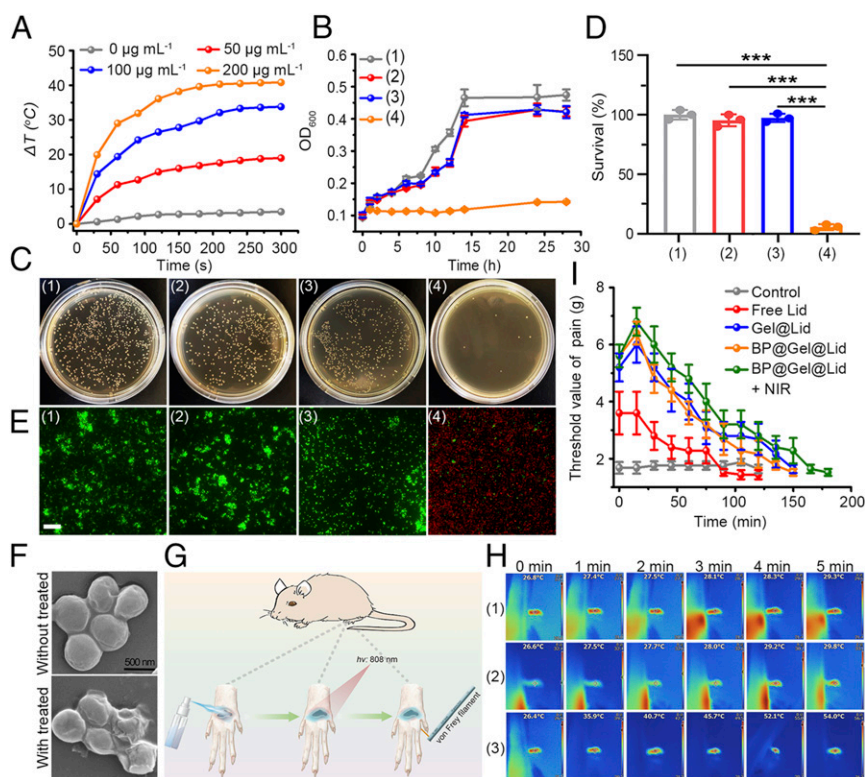
Ouyang et al.

www.manaraa.com

Fig. 4. BP-based gel eliminates bacteria through photothermal effects and provides on-demand pain relief in diabetic mice. (*A*) Photothermal curves of BP@Gel with different concentrations of BP NSs. (*B*) Growth profiles of SA bacteria with different treatments: (1) control, (2) NIR, (3) BP@Gel, and (4) BP@Gel + NIR. (*C*) Digital photographs of SA bacterial colonies grown on LB agar plates with different treatments and (*D*) corresponding quantitative measurement. (*E*) Bacterial membrane integrity was tested through calcein-AM/PI staining with different treatments. (Scale bar, 20 μm.) (*F*) SEM images of SA bacteria with or without PTT of BP@Gel. (*G*) Illustration of using von Frey filament to test the anesthetic effect of BP@Gel@Lid on mice. (*H*) Photothermal image of mice feet with different treatments of (1) BP@Gel@Lid, (2) NIR, and (3) BP@Gel@Lid + NIR. (*I*) The anesthetic effect of mice feet through mechanical allodynia caused by touching with von Frey filaments after different treatments. Data are means ± SE; *n* = 5. ***P < 0.001.

results also demonstrated that around 94.3% of bacteria were eliminated after SA was treated with BP@Gel under NIR laser irradiation (Fig. 4*D*), indicating superior antibacterial action. We next explored the mechanism underlying the antibacterial effects of BP@Gel by examining SA membrane integrity. A membrane-impermeable dye, propidium iodide, which can penetrate only damaged bacteria and bind with nucleic acids to generate red fluorescence, was utilized. Meanwhile, calcein-AM with green fluorescence was used to determine the structural integrity of bacterial membranes. For treatment with Gel or BP@Gel alone, almost all of the bacteria were stained by calcein-AM and emitted green fluorescence, which was nearly the same as the control group, indicating the integrity of membrane structure. In contrast, almost all bacteria lost their membrane integrity and emitted red fluorescence after treatment with BP@Gel under NIR laser irradiation (Fig. 4*E*). We speculated the reason for rapid bacterial membrane rupture was likely local hyperthermia induced by the robust photothermal effect of BP@Gel. Afterward, the integrity of the bacterial membrane was examined by SEM (Fig. 4*F*). Morphology featuring an intact spherical structure with a smooth surface was observed in the normal SA bacteria. After treatment with BP@Gel under NIR laser irradiation, the SA cell membranes were seriously compromised, with obvious surface collapse. Therefore, BP@Gel with the photothermal effect mediated by NIR produces rapid sterilization by destroying the bacterial membrane.

BP-Based Gel Could Act as an Anesthetic Drug "Reservoir" to Provide On-Demand Pain Relief in Diabetic Mice. A proportion of DU patients may always suffer severe pain, and alleviating their pain

remains a major challenge for these patients (9). Lid is a classic local anesthetic widely applied in the treatment of chronic and acute pain (35) whose degradation product is deethylated intermediate metabolites of monoethylglycinexylidide, which would be eventually hydrolyzed by amidase and discharges through urine without causing obvious side effects (36, 37). To incorporate a pain-relief function, Lid was loaded into the BP-based gel for DU treatment in diabetic mice. The release behavior of Lid from hydrogel was evaluated, and an NIR-triggered increased release was observed (*SI Appendix*, Fig. S10*A*). It is worth mentioning that, although the fibrin gel is not a typical thermosensitive hydrogel, BP NSs have NIR-responsive properties, which endows the gel with an NIR-triggered increased Lid release behavior. This NIR-responsive release is likely caused by the mild loose structure of the gel under the photothermal effect of BP NSs (*SI Appendix*, Fig. S9*C*). Furthermore, the in vivo anesthesia behavior of Gel@Lid and BP@Gel@Lid was investigated through a von Frey test. The diabetic mice models were established through intraperitoneal (i.p.) injection of streptozocin (STZ), and the mice with blood glucose levels above 16.7 mM were regarded as diabetic mice (*SI Appendix*, Fig. S11). A wound was created on the right rear instep of diabetic mice, and hydrogel containing different components or free Lid was then sprayed on the wound beds (Fig. 4*G*). Afterward, the wounds were irradiated with or without NIR. Photothermal images of temperature changes in mice feet are shown in Fig. 4*H*. After the animals were treated with Gel@BP@Lid and NIR irradiation, the local temperature of mice feet increased rapidly to 54 °C (*SI Appendix*, Fig. S12), which is much higher than body surface

Ouyang et al.

www.manaraa.com

temperature, accelerating the release of Lid. Subsequently, von Frey filaments were used to stimulate the midplantar skin to evaluate the pain reaction. The bending force necessary to elicit paw withdrawal was measured; a stronger bending force manifested deeper anesthesia. The strongest bending force was 8 g, and the threshold in untreated mice was 1.4 g. Only 60% of the mice treated with free Lid displayed an anesthetic effect, and the analgesia only lasted 75 min (Fig. 4*I* and *SI Appendix*, Fig. S10*B*). Significant anesthetic effects were observed for all mice treated with hydrogel, and the analgesia in both Gel@Lid and Gel@BP@Lid groups lasted longer than in the free Lid group, up to 120 min and 135 min, respectively. The inherent nature of hydrogel allows it to serve as a "reservoir," holding the Lid solution, releasing it slowly, and increasing the area of contact with the wound to extend anesthetic time. Notably, mice with Gel@BP@Lid and NIR irradiation treatment exhibited longer analgesia, >150 min, nearly twice the duration of the Lid group, due to the enhanced Lid release triggered by NIR. These results suggest that the BP-based gel can serve as a reservoir to load anesthetic drugs to achieve prolonged and on-demand local analgesia.

BP-Based Gel Accelerates Wound Healing, Promotes Angiogenesis, Eliminates Bacteria, and Reduces Inflammation in Diabetic Mice. Based on the encouraging pain relief results, we investigated the therapeutic effects of our engineered BP-based gel for DU treatment in the diabetic mouse model with infected wounds. The infected diabetic mice were randomly divided into four groups: G1, control; G2, Gel; G3, BP@Gel; and G4, BP@Gel@Lid + NIR. After the mice received the above treatments, the in vivo photothermal effect of BP@Gel was evaluated through thermal imaging (Fig. 5*A*). For the mice with BP@Gel treatment, the temperature at infected sites increased by 26.5 °C under NIR laser irradiation (Fig. 5*B*), indicating the excellent in vivo photothermal property of BP@Gel. Meanwhile, the local temperature in the mice treated with NIR laser only or BP@Gel alone did not undergo obvious changes (Fig. 5*B*). To assess wound healing efficacy, the wounds with bacterial infection were monitored over time. On day 10, the mice in G4 exhibited the best wound healing, while visible scars still remained in other groups, and distinct scabs were found in the control group (Fig. 5*C*). The wound healing rate curve also demonstrated that the wound healing of mice in G4 (almost complete healing) was much faster than in the other groups, especially compared with the control group (Fig. 5*D*). Furthermore, for G4, an average of 5.7 d later the wound area was reduced to 50% of its original size, while G1 required 9.3 d to recover half of the wound (Fig. 5*E*). Notably, after 10 d, the wound area in G4 was 5.44, 2.25, and 2.23 times smaller than that of G1, G2, and G3, respectively (Fig. 5*F*), suggesting the excellent wound healing ability of our NIR-responsive BP-based gel.

Wound healing is a complex process involving a series of biological phases that include hemostasis, inflammation, migration, proliferation, reepithelialization, and maturation (38). Hence, hematoxylin and eosin (H&E) and Masson's trichrome staining were performed to study the mechanism behind this process. As shown in Fig. 5*G*, on day 4 there was an obvious boundary between normal tissue and the wound in all treatment groups. Abundant inflammatory cells were present and most collagen fibers were lost in G1, G2, and G3 (#1 in Figs. 5 *G* and *H* and 6*A*). In comparison, a basic epithelial structure and ample collagen fibers were found in the wound sites of G4 and the collagen deposition area was about 61% vs. only 35% for the control group (G1). Moreover, there were significantly fewer inflammatory cells in G4 than in the other groups (#1 in Fig. 5*H*), which may be attributed to the bacterial reduction mediated by PTT with the BP-based gel. On day 8, G1 wound sites had formed a few collagen fibers, but plenty of inflammatory cells were still observed, and no obvious epithelial structure was present (*SI Appendix*, Fig.

S13*A*). However, for G2, G3, and G4, denser epithelium and granulation structures were found, especially in G4. Furthermore, a large number of inflammatory cells were noted in G2 and G3, clearly more than in G4. Two days after day 10, the mice were sacrificed, and the wound sections were checked on the endpoint of this study. In G1, although collagen fibers had increased and a thin epithelial structure formed, there was still a large space and a loose reticular arrangement between collagen fibers and skin tissue (#2 in Figs. 5*G* and 6*A*), and the collagen deposition area was still only 45% (#2 in Fig. 6*B*). Excessive inflammation was also one of the factors that delayed wound healing. There were significantly fewer inflammatory cells in G4 compared to the other groups (#2 in Fig. 5*H*). Notably, although more regular collagen fibers were formed in G2 and G3, abundant inflammatory cells were still present (#2 in Fig. 5*H*). Conversely, an entire epidermal structure and compact, regular collagen fibers were formed in G4, and the collagen deposition area reached 80% (#2 in Fig. 6*B*).

Wound healing requires oxygen, growth factors, nutrients, and so on. These substances are usually transported through the blood to penetrate the wound site (39). Therefore, neovascularization is essential for tissue regeneration, and insufficient local blood supply may prevent the wound from healing (40). CD31, a capillary marker, was selected to characterize the formation of microvessels through immunohistochemical staining (41). Compared with the control group (G1), neovascularization increased significantly in all of the hydrogel-treated groups on day 8 (#1 in Fig. 6 *C* and *D*). Simultaneously, microvessel formation gradually increased over time, but the untreated group still had sparse blood vessels, significantly fewer than the other groups, at the endpoint (#2 in Fig. 6 *C* and *D*).

Because of their exposure to air and high local glucose concentration, skin wounds in diabetic mice are prone to be teeming with bacteria (3). Furthermore, the infected environment can delay wound healing. Therefore, bacterial infection in different groups was evaluated through Giemsa staining. In G1, G2, and G3, large amounts of bacteria were present in the wound bed on day 4 (Fig. 6*E*), notably higher than in G4 (Fig. 6*F*), while some bacteria even remained at the endpoint (*SI Appendix*, Fig. S13*B*). In contrast, almost no staining bacteria were detected in group G4 (Fig. 6*E* and *SI Appendix*, Fig. S13*B*), which was attributed to the antibacterial performance mediated by the photothermal effect of the BP-based gel.

Taken all together, our findings demonstrate that the in situ sprayed NIR-responsive, pain relief BP-based gel developed in our study effectively achieved on-demand pain relief, accelerated wound healing, promoted angiogenesis, eliminated bacteria, and reduced inflammation in diabetic mice.

Discussion

As one of the most prevalent metabolic diseases, diabetes mellitus and its complications constitute serious health and economic problems worldwide (42, 43). Chronic DUs, which usually occur in the feet and legs (though also in other locations on the skin), have caused over 73,000 nontraumatic lower-limb amputations and imposed a substantial financial burden (about $9 to $13 billion) annually, in addition to the costs by diabetes itself (10). Furthermore, about nearly one-third of amputees would lose their contralateral limb in less than 3 y, and almost two-thirds of them would die less than 5 y after the amputation (44). Considering that 85% of all amputations in diabetes occur after an ulcer, the optimal care of DUs is of utmost importance to improve the quality of life for diabetic patients (45). However, complete and fast healing of DUs is challenging due to the tough wound healing environment created by diabetes (46). Despite the use of dressings including films, hydrocolloids, foams, alginates, and hydrogels to help protect the ulcer from injury and further infection, these materials are used mainly to create a moist and warm environment to promote wound repair (47). Few
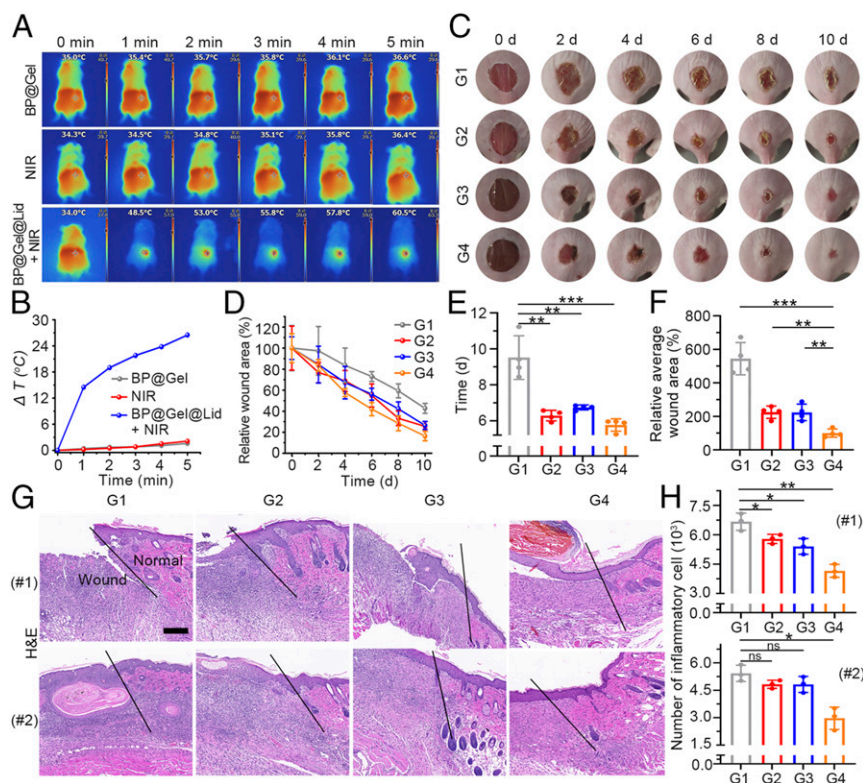
www.manaraa.com

Fig. 5. BP-based gel accelerates wound healing and reduces inflammation in diabetic mice. (*A*) Photothermal image of mice after treatment with BP@Gel, NIR, and BP@Gel@Lid + NIR. (*B*) Temperature changes of mice wound sites after different treatments. (*C*) Images of wound healing in mice skin at different times after different treatments: G1, control; G2, Gel; G3, BP@Gel; and G4, BP@Gel@Lid + NIR. (*D*) Relative wound area curves of mice after different treatments. (*E*) Time of wound healing to half of the wound area. (*F*) The relative average wound area of each group relative to the G4 group on day 10. (*G*) Representative H&E staining image of mice wound healing at different times: (#1) day 4 and (#2) endpoint. The left side of the black line represents normal tissue, and the right side of the black line represents the wound. (Scale bar, 200 μm.) (*H*) Quantitative analysis of inflammatory cells in G. *$P < 0.05$, **$P < 0.01$, and ***$P < 0.001$. ns, not statistically significant.

dressing materials are designed to activate cells associated with tissue repair for promoting wound healing. Furthermore, the complication of severe pain induced by DU also severely reduces the quality of life for the diabetes patient. There is growing evidence that chronic wounds have a huge impact on patients' quality of life, while one of the consistent opinions is that pain is particularly distressing as a major symptom in some DU patients (48–51). A wound represents a loss of skin integrity and cut nerve fibers, and therefore the resulting pain is attributed to a combination of pain caused by nerve damage (neuropathic pain) and nociceptive pain (51). Essentially, there are many broken nerve fibers distributed around the wound, especially for the patients with a diabetic foot ulcer; most of them often suffer from enormous foot pain due to the abundance of tactile nerves in the soles, which seriously affects their quality of life. Based on a questionnaire incorporating pain assessment, about 60% of DU patients suffered from neuropathic ulcers and 40% had neuroischaemic ulcers (52). Effective pain relief during DU treatment still presents a major clinical challenge. Therefore, developing effective regenerative dressings that can address these issues and promote wound closure is highly desirable.

The overall objective of this study was to target all of the complex and challenging wound-healing milieu associated with DUs, including chronic wounds, impaired angiogenesis, persistent pain, bacterial infection, and exacerbated inflammation. BP NSs were synthesized and incorporated into a fibrinogen solution with the FDA-approved anesthetic Lid. Simply by simultaneously spraying the therapeutics containing fibrinogen and thrombin, a BP-based solid gel could be formed on the DU sites to cover and

protect the wounds. The fibrin gel formed by the fibrinogen/thrombin interaction has demonstrated effectiveness for the ability to promote wound healing and postsurgical treatment (18, 19), while this degradable biopolymer formed from fibrinogen can be eventually degraded with plasmin-mediated fibrinolysis, which exhibits high biocompatibility (53). By engineering the gel with developed BP nanomaterials and Lid, we have created an NIR-responsive, pain-relieving treatment for chronic wounds in diabetes.

Among the emerging two-dimensional (2D) monoelemental materials (Xenes) (24, 54–58), BP is a biodegradable and biocompatible nanomaterial with PO_x^{3-} as the degradation product, which is harmless to the human body. BP has also been widely developed as a useful photothermal agent with different nanostructures (20, 59, 60). Photothermal treatment with such photothermal agents can be used for accelerating microcirculatory blood flow, mediating the release of drugs (23, 61) for "on-demand" pain relief, eliminating bacteria (24), and reducing inflammation (62). Although one concern is that local hyperthermia may cause burns to the skin around the wound, the damage to cells around the wound caused by PTT is far less serious than that caused by a bacterial infection, which is acceptable for the PTT-mediated wound healing. Furthermore, BP also easily degrades to nontoxic phosphate and phosphonates, improving the safety of photothermal treatment (63–65). Despite recent studies focused on impressive new applications of BP nanomaterials in cancer treatment (20, 22, 23), bone regeneration, and neurodegenerative disorder therapy (21, 54), their application in treating DUs has rarely been explored. Therefore,
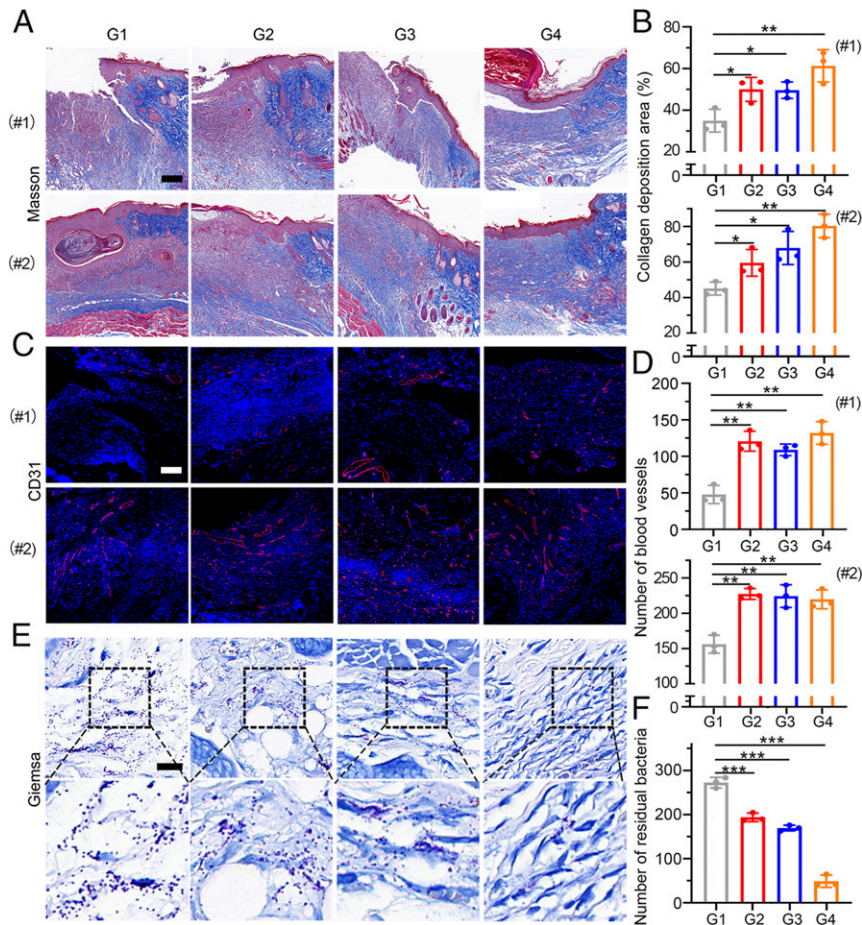
Fig. 6. BP-based gel promotes angiogenesis and eliminates bacteria in diabetic mice. (*A*) Representative Masson staining image of mice wound healing at different times: (#1) day 4 and (#2) endpoint. (Scale bar, 200 μm.) (*B*) Quantitation of collagen deposition area in *A*. (*C*) Immunofluorescence staining for CD31 in wound tissues at different times after treatments: (#1) day 8 and (#2) endpoint. (Scale bar, 200 μm.) (*D*) Quantification of blood vessels in *C*. (*E*) Giemsa staining of wound tissues after 4-d treatment. (Scale bar, 25 μm). (*F*) Quantification of residual bacteria in E. *$P < 0.05$, **$P < 0.01$, and ***$P < 0.001$.

our study also provides the proof-of-concept for the use of BP-based materials in DU treatment. Despite these mentioned advantages, there are still several limitations of this multifunctional hydrogel. The most important thing to discuss is the biosafety of BP NSs in humans. Although many studies have demonstrated that BP NSs (with nontoxic phosphate as the degradation product) are biodegradable and biocompatible, no clinical trial has been reported to confirm the biosafety of BP NSs in humans. How to prepare BP NSs with uniform sizes on a large scale may also need to be explored. Additionally, although BP NSs have NIR-responsive properties, the fibrin gel is not a thermosensitive hydrogel and the photothermal effect of BP NSs can only mildly promote the release of anesthetic drugs (Lid) in the gel. Future studies to deal with these problems may be needed to fulfill the true clinical application of this BP-based hydrogel.

In summary, our study provides proof-of-principle evidence for using an in situ sprayed, NIR-responsive, pain-relief BP-based gel for effective DU treatment. Both in vitro and in vivo results demonstrated that this BP-based gel simultaneously and effectively addresses individual features of the harsh wound healing milieu such as chronic wounds, impaired angiogenesis, persistent pain, bacterial infection, and exacerbated inflammation, suggesting the potential for significant improvements to the treatment of diabetic patients with ulcers. Moreover, this study may also shed light on the future development of pain relief nanotechnology in medical applications and greatly expand research areas for BP-based materials.

Materials and Methods

Materials. Bulk BP crystals (catalog no. 101127) were provided by HWRK Chemicals. HUVEC and D551 cells and SA strain ATCC25923 were obtained from the American Type Culture Collection. Fetal bovine serum (FBS, catalog no. 16140071), penicillin–streptomycin (catalog no. 15140122), Dulbecco's modified Eagle's medium (DMEM) culture medium (catalog no. 21013024), trypsin (catalog no. 25300054), FITC-phalloidin (catalog no. F432), DAPI (catalog no. D3571), propidium iodide (PI, catalog no. P1304MP), calcein-AM (catalog no. C1430), lysogeny broth (LB, Miller) powder microbial growth medium (catalog no. 12795027), and the Alexa Fluor 488 dye-labeled EdU cell proliferation kit (catalog no. C10337) were from Thermo Fisher Scientific. EBM-2 culture medium (catalog no. 00190860) was purchased from Lonza. The CCK-8 cell viability assay kit (catalog no. ab228554) was purchased from Abcam. Agarose (catalog no. A9045), sodium hydroxide (NaOH, catalog no. S8045), *N*-methyl-2-pyrrolidone (NMP, catalog no. 328634), Lid (catalog no. 1366013), fibrinogen (human, catalog no. F8630), and thrombin (human, catalog no. T1063) were purchased from Sigma-Aldrich. Other solvents and reagents were analytically pure and required no further purification before use.

Preparation of BP NSs. BP NSs were prepared based on our previously reported approach. Specifically, 2 g of NaOH was mixed with 45 mL of NMP, and the solution was sonicated for 5 min; the excess NaOH was removed to obtain a saturated NaOH solution in NMP, to which 20 mg of bulk BP powder was added. A probe sonicator (JY92-IIN; Scientz) was used for ice bath sonication treatment of the solution for 8 h, after which the solution was centrifuged (4,000 rpm, 10 min) and the unexfoliated bulk BP powder removed. The obtained supernatant was further centrifuged (13,000 rpm) for 10 min to collect BP NSs and washed with ultrapure water twice before use.

Ouyang et al.

www.manaraa.com

Formation of Fibrin Gel (Gel) and BP@Gel. To obtain the fibrin gel (Gel), fibrinogen solutions with and without BP NSs were mixed with a thrombin solution in equal volume through spraying. Hydrogels for different studies were obtained by adjusting the concentration of different substances. The concentration of fibrinogen solution and thrombin solution was 2.5 mg·mL^{-1} and 5 NIH U·mL^{-1}, respectively. For cell experiments, the final concentration of fibrinogen solution and thrombin solution was 2 mg·mL^{-1} and 2 NIH U·mL^{-1}, respectively. Fibrinogen solution at a final concentration of 2.5 mg·mL^{-1} and thrombin solution at a final concentration of 5 NIH U·mL^{-1} was used for in vitro antibacterial experiments. For animal experiments, the final concentrations of fibrinogen solution and thrombin solution were 10 mg·mL^{-1} and 10 NIH U·mL^{-1}, respectively. The concentration of BP NSs in all cell experiments was 50 μg·mL^{-1}. For the other experiments, the concentration of BP NSs was 100 μg·mL^{-1}.

Characterization. TEM (Tecnai G2; FEI) and AFM (Veeco; NanoMan) were used to examine the morphology of BP NSs. An SEM (S-4800; Hitachi) was used to characterize the microstructure of Gel and BP@Gel. A Raman microspectrometer (HR 800; Jobin Yvon LabRam-010) was utilized to conduct Raman scattering. An X-ray automatic diffractometer (D500; Siemens) was used for XRD. XPS spectra were obtained using a photoelectron spectrometer (ESCALAB 250; Thermo Fisher). A UV-2450 spectrophotometer (Shimadzu) was employed to record ultraviolet-visible (UV-vis) absorbance.

Cell Culture. D551 cells were incubated in DMEM, and EBM-2 medium was used for HUVEC incubation. Streptomycin/penicillin (1%) and FBS (10%) were added to DMEM and EBM-2 medium as supplements. Furthermore, the supplements of human epidermal growth factor B (0.4%), vascular endothelial growth factor (0.1%), arginine 3 insulin-like growth factor 1 (0.1%), human epidermal growth factor (hEGF) (0.1%), GA-1000 (0.1%), and heparin (0.1%) were added into EBM-2 medium. Both the D551 cells and HUVECs were incubated in an atmosphere of 5% CO$_2$ at 37 °C.

Cell Survival Study and EdU Proliferation Assay. For the cell survival study, 100 μL of thrombin solution was added into each well of a 24-well plate, then an equal volume of fibrinogen solution (with or without BP NSs) was added. About 10 min later, the fibrin gel had formed. Subsequently, D551 cells and HUVECs were seeded onto the surface of the Gel or BP@Gel at a density of 1.5 × 10^4 per well, respectively. After 1 d or 3 d incubation, the medium was removed and CCK-8 diluent was added to determine cell survival. For the EdU proliferation assay, the cells received the above treatment and were then stained according to the manufacturer's protocol. The stained cells were further imaged using an inverted fluorescence microscope.

Fibrin Bead Assay. The culture medium of HUVECs and D551 cells was changed to EGM-2 medium at least 1 d before use of the cells. Then, HUVECs were mixed with Cytodex-3 microcarriers at a density of ~400 HUVECs per bead. The tube containing cells and beads was incubated at 37 °C for 4 h. During incubation, the tube was gently inverted and mixed every 20 min. After the beads were coated by HUVECs, the beads resembled golf balls under a microscope. Afterward, the coated beads were transferred to a T25 tissue culture flask and further cultured overnight in the incubator in an atmosphere of 5% CO$_2$ at 37 °C. The coated beads were washed with EMG-2 twice and then mixed with fibrinogen or BP/fibrinogen solution at a concentration of 400 beads per mL. Thrombin stock solution (250 μL) was added into each well of a 24-well plate, and then 250 μL of fibrinogen solution containing coated beads were mixed with the above thrombin solution. The fibrinogen/bead solution was placed in the clean bench to clot for 5 min at room temperature. During the first 5 min of solidification, the 24-well plate was held still to avoid tearing of the fibrin gel. After 5 min, the 24-well plate was transferred to the incubator and further clotted for 15 min at 37 °C and 5% CO$_2$. Meanwhile, D551 cells were trypsinized and resuspended in EGM-2 at a density of 2 × 10^4 cells per mL. Afterward, 1 mL of D551 cell suspension was added to each well (on top of the fibrin gel) drop by drop, because it is easy to tear the fibrin gel through rapid addition. Every other day, the medium was removed and replaced with fresh EGM-2 medium. During incubation, a microscope was used to observe the formation of microvessel-like structures and capture the desired images. At about 7 d, the formed microvessel-like structures were stained for DAPI and phalloidin-TRITC. Specifically, 4% paraformaldehyde (500 μL) was added to the gels at 37 °C for 2 h to stop the assay, followed by overnight incubation at room temperature to fix the microvessel structures. The gels were then washed with phosphate-buffered saline (PBS) twice, and 0.5% Triton X-100 (500 μL) was added for 20 min to permeabilize them. After that, the gels were washed with PBS twice and further incubated with 5% bovine serum albumin solution (500 μL) for 0.5 h.

Five hundred microliters of the mixture of Hoechst 33258 and phalloidin-FITC in PBS was cultured for 2 h. After two washes with PBS, an inverted fluorescence microscope was used to image the microvessel structures.

In Vitro HUVECs Migration Assay. HUVECs were seeded into 12-well plates at a density of 3 × 10^4 per well. After overnight incubation, a straight scratch was created by pipette tip (1 mL), and the cells were gently washed twice with the medium. A Transwell containing Gel or BP@Gel was placed in each well. After 54 h of culture, HUVECs were fixed with paraformaldehyde and further stained with trypan blue. Afterward, the cells were washed with PBS twice and imaged using a microscope. The relative wound area was calculated based on the following equation: wound area (%) = $(W_0 - W_{54\,h})/W_0$, where $W_{54\,h}$ was the wound area after 54 h of incubation and W_0 was the initial wound area.

Photothermal Effect of BP@Gel. To form BP@Gel, fibrinogen solutions containing different concentrations of BP NSs (50, 100, or 200 μg·mL^{-1}) were mixed with thrombin solution in equal volume through spraying. After 30 min, BP@Gel was exposed to the 808-nm laser with different power densities (0.5, 1, 1.5, or 2 W·cm^{-2}) for 5 min. The temperature changes of BP@Gel were recorded using a thermal infrared imaging camera (Flir C2).

Antibacterial Activity of BP@Gel. SA bacteria were incubated in LB medium for 24 h at 37 °C and then mixed with Gel or BP@Gel (BP NSs, 100 μg·mL^{-1}) in a transparent vial at a density of 1 × 10^6 colony-forming units (CFU) per mL. Afterward, SA bacteria were divided into four groups: 1) control, 2) Gel, 3) BP@Gel, and 4) BP@Gel + NIR. For group 4, the bacteria received 10-min irradiation treatment by 808-nm laser at a power density of 1 W·cm^{-2} and were incubated for another 28 h. The absorbance of 600 nm (OD$_{600\,nm}$) at different time points was recorded to determine bacterial growth. In addition, bacterial survival and density were quantified through the agar plate assay. For the bacterial membrane integrity study, SA bacteria that received the above treatment were stained with PI and calcein-AM for 1 h. The SA bacteria were then centrifuged, collected, and washed twice with PBS for fluorescence imaging.

SEM Images of Bacterial Morphology. An SA bacteria suspension at a density of 1 × 10^6 CFU per mL was added to a transparent vial containing BP@Gel (BP NSs, 100 μg·mL^{-1}) and irradiated under 808-nm laser for 10 min at a density of 1 W·cm^{-2}. After centrifugation, the bacteria were collected and fixed with paraformaldehyde. Afterward, the fixed bacteria were further dehydrated by successive treatment with 10, 25, 50, 75, 90, and 100% ethanol for 15 min. The bacterial suspension was then dropped onto a silicon wafer and imaged using SEM to examine the morphology of the bacteria after drying.

In Vitro Lid Release. Thrombin solution (500 mL) was placed in a 20-mL vial, and then an equal volume of fibrinogen solution containing Lid (20 mg·mL^{-1}) as well as BP NSs (100 μg·mL^{-1}) was mixed with the thrombin solution to form a thin fibrin gel at the bottom of the vial. After 10 min, 4 mL of PBS solution with a pH of 7.4 was added to the vial. Afterward, vials containing hydrogels were placed in a shaking incubator at 37 °C; 20 μL of the solution was removed from the vial at different time points to evaluate Lid release. Furthermore, to study NIR-triggered Lid release, the processes were performed under the same conditions. Meanwhile, before the samples were removed from the vial at different time points, the hydrogels were exposed to 808-nm laser (1 W·cm^{-2}) for 5 min. The concentration of obtained samples was quantified by high-performance liquid chromatography by the following method: column: C18; mobile phase: MeCN 40% with 0.1% H$_3$PO$_4$; detection: UV 270 nm; flow rate: 1 mL·min^{-1}.

Animal Experiments. Male BALB/c mice (6 wk old) were purchased from Charles River Laboratories. All animal experiments were executed according to NIH's *Guide for the Care and Use of Laboratory Animals* (66) under sterile conditions at the animal facility of Brigham and Women's Hospital. All experimental protocols were approved under the guidelines of the Institutional Animal Care and Use Committees at Harvard Medical School.

Establishment of the Diabetic Model in Mice. Male BALB/c mice (6 wk old) were administered STZ (50 mg·kg^{-1}) through i.p. injection for five consecutive days to establish the diabetic mouse model (67–69). The blood glucose of the mice was monitored using a glucometer. Mice with blood glucose levels <16.7 mM were excluded, and the rest were confirmed diabetic mice.

In Vivo Behavioral Testing Study. Diabetic mice were anesthetized by isoflurane, and a circular cut (3.5 mm × 3.5 mm) was created on the right rear instep using a scissor. Lid was then mixed with fibrin gels or BP/fibrin gels

Ouyang et al.

and sprayed using a dual-cartridge sprayer to cover the wound. Meanwhile, the Lid solution was also dropped onto the wound to compare the anesthesia results with fibrin gels. The mice were divided into five groups (five mice per group): G1: control, G2: Lid, G3: Gel@Lid, G4: BP@Gel@Lid, and G5: BP@Gel@Lid + NIR. After spraying for 10 min, the von Frey test was performed to assess the mechanical allodynia of mice. Afterward, the von Frey test was executed every 15 min. For group G5, wounds were irradiated with 808-nm laser at a density of 1 W·cm^{-2} for 5 min at the second test and temperature changes recorded via thermal infrared imaging camera. Mice were placed on a wire mesh floor, and then using von Frey filaments (The Touch Test Sensory Evaluator Set; Linton Instrumentation) bending force ranging from 1 to 15 g was used to stimulate the midplantar skin of each hind paw for 6 s. The bending force that forced the mice to exhibit a withdrawal response was the effective strength. A modified approach according to previous reports was used to determine the 50% paw withdrawal thresholds (70, 71). First, the mouse hind paws were stimulated using von Frey filaments beginning at 1 g, up to the strength required to force mice to show the withdrawal response. Next, the hind paws were stimulated using von Frey filaments beginning at 15 g down and decreasing to the strength at which mice did not show the withdrawal response. These up-and-down processes were repeated five times. The average of the weakest force in each up or down step was the effective 50% threshold.

Diabetic Skin Wound Healing In Vivo. Diabetic mice were anesthetized by isoflurane, and a round wound (diameter: 7 mm) was made on the back of the mice using scissors. Fifty microliters of SA saline (1 × 10^9 CFUs per mL) was then dropped onto the wound to induce diabetic skin infection. After 15 min, the infected wound was washed with a PBS solution twice. Immediately, fibrin gels containing different formulations (Gel, BP@Gel, or BP@Gel@Lid) were sprayed on to cover the wound via a dual-cartridge sprayer. Meanwhile, the mice were divided into four groups: G1, control; G2, Gel; G3, BP@Gel; and G4, BP@Gel@Lid + NIR group. For G4, the mice were irradiated with NIR laser (808 nm, 1 W·cm^{-2}) for 5 min and temperature changes recorded with a thermal infrared imaging camera. Untreated SA-infected mice served as controls. Wounds were photographed every 2 d, and the length and the width were recorded to calculate the area. Representative mice in each group were sacrificed at 4, 8, and 12 d, and the wounded skin was collected for histological and immunofluorescent staining.

Statistical Analysis. Origin 9 and GraphPad Prism 8 were used for all statistical analyses, and images were analyzed by ImageJ. Multiple t tests or two-way ANOVA were performed during the statistical analysis. All studies were carried out at least in triplicate, and all data were calculated as mean ± SD unless otherwise stated. A value of $P < 0.05$ is considered statistically significant, where all statistically significant values shown in the figures are indicated as *$P < 0.05$, **$P < 0.01$, and ***$P < 0.001$.

Data Availability. All data are available within this manuscript and the associated *SI Appendix*. Additional data are available from the corresponding author on reasonable request.

1. S. A. Eming, P. Martin, M. Tomic-Canic, Wound repair and regeneration: Mechanisms, signaling, and translation. *Sci. Transl. Med.* **6**, 265sr6 (2014).
2. P. C. Leung, Diabetic foot ulcers–A comprehensive review. *Surgeon* **5**, 219–231 (2007).
3. S. E. Dowd et al., Polymicrobial nature of chronic diabetic foot ulcer biofilm infections determined using bacterial tag encoded FLX amplicon pyrosequencing (bTEFAP). *PLoS One* **3**, e3326 (2008).
4. A. L. Calle-Pascual et al., Nontraumatic lower extremity amputations in diabetic and non-diabetic subjects in Madrid, Spain. *Diabetes Metab.* **23**, 519–523 (1997).
5. H. Thangarajah et al., The molecular basis for impaired hypoxia-induced VEGF expression in diabetic tissues. *Proc. Natl. Acad. Sci. U.S.A.* **106**, 13505–13510 (2009).
6. V. Falanga, Wound healing and its impairment in the diabetic foot. *Lancet* **366**, 1736–1743 (2005).
7. J. E. Patterson, V. T. Andriole, Bacterial urinary tract infections in diabetes. *Clin. Infect. Dis.* **11**, 735–750 (1997).
8. L. J. Wheat, Infection and diabetes mellitus. *Diabetes Care* **3**, 187–197 (1980).
9. A. Veves, C. Manes, H. J. Murray, M. J. Young, A. J. Boulton, Painful neuropathy and foot ulceration in diabetic patients. *Diabetes Care* **16**, 1187–1189 (1993).
10. J. Xiao, S. Chen, J. Yi, H. Zhang, G. A. Ameer, A cooperative copper metal–organic framework-hydrogel system improves wound healing in diabetes. *Adv. Funct. Mater.* **27**, 1604872 (2017).
11. T. G. Ebrahimian et al., Cell therapy based on adipose tissue-derived stromal cells promotes physiological and pathological wound healing. *Atertio. Thromb. Vasc. Biol.* **29**, 503–510 (2009).
12. R. G. Frykberg, J. Banks, Challenges in the treatment of chronic wounds. *Adv. Wound Care (New Rochelle)* **4**, 560–582 (2015).
13. H. Chen et al., An injectable self-healing coordinative hydrogel with antibacterial and angiogenic properties for diabetic skin wound repair. *NPG Asia Mater.* **11**, 1–12 (2019).
14. Y. Zhao et al., Skin-inspired antibacterial conductive hydrogels for epidermal sensors and diabetic foot wound dressings. *Adv. Funct. Mater.* **29**, 1901474 (2019).
15. H. Wu, F. Li, W. Shao, J. Gao, D. Ling, Promoting angiogenesis in oxidative diabetic wound microenvironment using a nanozyme-reinforced self-protecting hydrogel. *ACS Cent. Sci.* **5**, 477–485 (2019).
16. Y. Zhu et al., Potent laminin-inspired antioxidant regenerative dressing accelerates wound healing in diabetes. *Proc. Natl. Acad. Sci. U.S.A.* **115**, 6816–6821 (2018).
17. E. Vågesjö et al., Accelerated wound healing in mice by on-site production and delivery of CXCL12 by transformed lactic acid bacteria. *Proc. Natl. Acad. Sci. U.S.A.* **115**, 1895–1900 (2018).
18. Q. Chen et al., In situ sprayed bioresponsive immunotherapeutic gel for post-surgical cancer treatment. *Nat. Nanotechnol.* **14**, 89–97 (2019).
19. P. Martin, Wound healing–Aiming for perfect skin regeneration. *Science* **276**, 75–81 (1997).
20. N. Kong et al., ROS-mediated selective killing effect of black phosphorus: Mechanistic understanding and its guidance for safe biomedical applications. *Nano Lett.* **20**, 3943–3955 (2020).
21. Z. Tang et al., Phosphorus science-oriented design and synthesis of multifunctional nanomaterials for biomedical applications. *Matter* **2**, 297–322 (2020).
22. K. Hu et al., Marriage of black phosphorus and Cu^{2+} as effective photothermal agents for PET-guided combination cancer therapy. *Nat. Commun.* **11**, 2778 (2020).
23. W. Tao et al., Black phosphorus nanosheets as a robust delivery platform for cancer theranostics. *Adv. Mater.* **29**, 1603276 (2017).
24. C. Feng et al., Germanene-Based Theranostic Materials for Surgical Adjuvant Treatment: Inhibiting Tumor Recurrence and Wound Infection. *Matter* **3**, 127–144 (2020).
25. W. Chen et al., Black phosphorus nanosheet-based drug delivery system for synergistic photodynamic/photothermal/chemotherapy of cancer. *Adv. Mater.* **29**, 1603864 (2017).
26. O. Chaudhuri et al., Hydrogels with tunable stress relaxation regulate stem cell fate and activity. *Nat. Mater.* **15**, 326–334 (2016).
27. H. Ma, Q. Zhou, J. Chang, C. Wu, Grape seed-inspired smart hydrogel scaffolds for melanoma therapy and wound healing. *ACS Nano* **13**, 4302–4311 (2019).
28. K. M. Pawelec, S. M. Best, R. E. Cameron, R. J. Wardale, Scaffold architecture and fibrin gels promote meniscal cell proliferation. *APL Mater.* **3**, 014901 (2015).
29. W. Weng et al., Aligned carbon nanotubes reduce hypertrophic scar via regulating cell behavior. *ACS Nano* **12**, 7601–7612 (2018).
30. M. G. Tonnesen, X. Feng, R. A. F. Clark, Angiogenesis in wound healing. *J. Invest. Derm. Symp. P.* **5**, 40–46 (2000).
31. M. N. Nakatsu et al., Angiogenic sprouting and capillary lumen formation modeled by human umbilical vein endothelial cells (HUVEC) in fibrin gels: The role of fibroblasts and angiopoietin-1. *Microvasc. Res.* **66**, 102–112 (2003).
32. J. Li, Y.-P. Zhang, R. S. Kirsner, Angiogenesis in wound repair: Angiogenic growth factors and the extracellular matrix. *Microsc. Res. Tech.* **60**, 107–114 (2003).
33. A. M. Goodwin, In vitro assays of angiogenesis for assessment of angiogenic and anti-angiogenic agents. *Microvasc. Res.* **74**, 172–183 (2007).
34. Q. Wu, M. Liang, S. Zhang, X. Liu, F. Wang, Development of functional black phosphorus nanosheets with remarkable catalytic and antibacterial performance. *Nanoscale* **10**, 10428–10435 (2018).
35. W. G. Brose, M. J. Cousins, Subcutaneous lidocaine for treatment of neuropathic cancer pain. *Pain* **45**, 145–148 (1991).
36. J. M. Kenkel et al., Pharmacokinetics and safety of lidocaine and monoethylglycinexylidide in liposuction: A microdialysis study. *Plast. Reconstr. Surg.* **114**, 516–524, discussion 525–526 (2004).
37. N. Milman, M. Laub, E. P. Munch, H. R. Angelo, Serum concentrations of lignocaine and its metabolite monoethylglycinexylidide during fibre-optic bronchoscopy in local anaesthesia. *Respir. Med.* **92**, 40–43 (1998).
38. D. Brett, A review of collagen and collagen-based wound dressings. *Wounds* **20**, 347–356 (2008).
39. V. Moulin, Growth factors in skin wound healing. *Eur. J. Cell Biol.* **68**, 1–7 (1995).
40. M. Nomi, A. Atala, P. D. Coppi, S. Soker, Principals of neovascularization for tissue engineering. *Mol. Aspects Med.* **23**, 463–483 (2002).
41. Y. Xue, X. Xu, X.-Q. Zhang, O. C. Farokhzad, R. Langer, Preventing diet-induced obesity in mice by adipose tissue transformation and angiogenesis using targeted nanoparticles. *Proc. Natl. Acad. Sci. U.S.A.* **113**, 5552–5557 (2016).
42. N. C. Carrejo et al., Multidomain peptide hydrogel accelerates healing of full-thickness wounds in diabetic mice. *ACS Biomater. Sci. Eng.* **4**, 1386–1396 (2018).
43. L. Zhao et al., pH and glucose dual-responsive injectable hydrogels with insulin and fibroblasts as bioactive dressings for diabetic wound healing. *ACS Appl. Mater. Interfaces* **9**, 37563–37574 (2017).

44. J. R. Martin et al., Local delivery of PHD2 siRNA from ROS-degradable scaffolds to promote diabetic wound healing. Adv. Healthc. Mater. 5, 2751–2757 (2016).

45. D. G. Armstrong, A. J. M. Boulton, S. A. Bus, Diabetic foot ulcers and their recurrence. N. Engl. J. Med. 376, 2367–2375 (2017).

46. M. Lee, S. H. Han, W. J. Choi, K. H. Chung, J. W. Lee, Hyaluronic acid dressing (healoderm) in the treatment of diabetic foot ulcer: A prospective, randomized, placebo-controlled, single-center study. Wound Repair Regen. 24, 581–588 (2016).

47. W. J. Jeffcoate, K. G. Harding, Diabetic foot ulcers. Lancet 361, 1545–1551 (2003).

48. L. Ribu, A. Wahl, Living with diabetic foot ulcers: A life of fear, restrictions, and pain. Ostomy Wound Manage. 50, 57–67 (2004).

49. A. Hopkins, Disrupted lives: Investigating coping strategies for non-healing leg ulcers. Br. J. Nurs. 13, 556–563 (2004).

50. A. B. Wilson, Quality of life and leg ulceration from the patient's perspective. Br. J. Nurs. 13, S17–S20 (2004).

51. P. E. Price et al., Dressing-related pain in patients with chronic wounds: An international patient perspective. Int. Wound J. 5, 159–171 (2008).

52. A. Dickinson, N. Frescos, J. Firth, P. Hamblin, The characteristics of wound pain associated with diabetes-related foot ulcers: A pilot study. Wound Pract. Res. 24, 138–148 (2016).

53. Y. Li, H. Meng, Y. Liu, B. P. Lee, Fibrin gel as an injectable biodegradable scaffold and cell carrier for tissue engineering. Sci. World J. 2015, 685690 (2015).

54. W. Tao et al., Emerging two-dimensional monoelemental materials (Xenes) for biomedical applications. Chem. Soc. Rev. 48, 2891–2912 (2019).

55. J. Ouyang et al., 2D monoelemental germanene quantum dots: synthesis as robust photothermal agents for photonic cancer nanomedicine. Angew. Chem. Int. Ed. 131, 13539–13544 (2019).

56. T. Wei et al., Antimonene Quantum Dots: Synthesis and Application as Near-Infrared Photothermal Agents for Effective Cancer Therapy. Angew. Chem. Int. Ed. 56, 11896–11900 (2017).

57. W. Tao et al., Two-Dimensional Antimonene-Based Photonic Nanomedicine for Cancer Theranostics. Adv. Mater. 30, 1802061 (2018).

58. C. Liu, H. S. Kim, H. Won, E. Jung, J. S. Kim, Navigating 2D Monoelemental Materials (Xenes) for Cancer Nanomedicine. Matter 3, 12–13 (2020).

59. Z. Sun et al., Ultrasmall black phosphorus quantum dots: Synthesis and use as photothermal agents. Angew. Chem. Int. Ed. 54, 11526–11530 (2015).

60. J. R. Choi et al., Black phosphorus and its biomedical applications. Theranostics 8, 1005–1026 (2018).

61. M. Qiu et al., Novel concept of the smart NIR-light-controlled drug release of black phosphorus nanostructure for cancer therapy. Proc. Natl. Acad. Sci. U.S.A. 115, 501–506 (2018).

62. J. Ouyang et al., A black phosphorus based synergistic antibacterial platform against drug resistant bacteria. J. Mater. Chem. B 6, 6302–6310 (2018).

63. J. Plutnar, Z. Sofer, M. Pumera, Products of degradation of black phosphorus in protic solvents. ACS Nano 12, 8390–8396 (2018).

64. G. Abellán et al., Fundamental insights into the degradation and stabilization of thin layer black phosphorus. J. Am. Chem. Soc. 139, 10432–10440 (2017).

65. T. Zhang et al., Degradation chemistry and stabilization of exfoliated few-layer black phosphorus in water. J. Am. Chem. Soc. 140, 7561–7567 (2018).

66. National Research Council, Guide for the Care and Use of Laboratory Animals (National Academies Press, Washington, DC, ed. 8, 2011).

67. Y.-C. Tay et al., Can murine diabetic nephropathy be separated from superimposed acute renal failure? Kidney Int. 68, 391–398 (2005).

68. N. Sun, G. Yang, H. Zhao, H. F. J. Savelkoul, L. An, Multidose streptozotocin induction of diabetes in BALB/c mice induces a dominant oxidative macrophage and a conversion of TH1 to TH2 phenotypes during disease progression. Mediators Inflamm. 2005, 202–209 (2005).

69. A. A. Hardikar, M. S. Karandikar, R. R. Bhonde, Effect of partial pancreatectomy on diabetic status in BALB/c mice. J. Endocrinol. 162, 189–195 (1999).

70. T. Kawashiri et al., Prevention of oxaliplatin-induced mechanical allodynia and neurodegeneration by neurotropin in the rat model. Eur. J. Pain 15, 344–350 (2011).

71. S. R. Chaplan, F. W. Bach, J. W. Pogrel, J. M. Chung, T. L. Yaksh, Quantitative assessment of tactile allodynia in the rat paw. J. Neurosci. Methods 53, 55–63 (1994).

ENGINEERING

APPLIED BIOLOGICAL SCIENCES

Ouyang et al.